Crystals **2012**, *2*, 193-212; doi:10.3390/cryst2020193

OPEN ACCESS

crystals

ISSN 2073-4352

www.mdpi.com/journal/crystals

Article

Ammonia Uptake and Release in the MnX_2–NH_3 (X = Cl, Br) Systems and Structure of the $Mn(NH_3)_nX_2$ (n = 6, 2) Ammines

Hazel Reardon, James M. Hanlon, Michael Grant, Imogen Fullbrook and Duncan H. Gregory *

WestCHEM, School of Chemistry, University of Glasgow, Joseph Black Building, Glasgow G12 8QQ, UK; E-Mails: hazelr@chem.gla.ac.uk (H.R.); jamhan@chem.gla.ac.uk (J.M.H.); michaelgrant262@gmail.com (M.G.); 0706652f@student.gla.ac.uk (I.F.)

***** Author to whom correspondence should be addressed; E-Mail: duncan.gregory@glasgow.ac.uk; Tel.: +44-141-330-6438; Fax: +44-141-330-4888.

Received: 21 February 2012; in revised form: 18 March 2012 / Accepted: 30 March 2012 / Published: 10 April 2012

Abstract: Hexa-ammine complexes, $Mn(NH_3)_6X_2$ (X = Cl, Br), have been synthesized by ammoniation of the corresponding transition metal halide and characterized by Powder X-ray diffraction (PXRD) and Raman spectroscopy. The hexa-ammine complexes are isostructural (Cubic, *Fm*-3*m*, Z = 4; a = 10.2742(6) Å and 10.527(1) Å for X = Cl, Br respectively). Temperature programmed desorption (TPD) demonstrated that ammonia release from $Mn(NH_3)_6X_2$ complexes occurred in three stages corresponding to the release of 4, 1 and 1 NH_3 equivalents respectively. The chloride and bromide both exhibit a deammoniation onset temperature below 323 K. The di-ammoniates from the first desorption step were isolated during TPD measurements and their crystal structures determined by Rietveld refinement against PXRD data (X = Cl: orthorhombic *Cmmm*, a = 8.1991(9) Å, b = 8.2498(7) Å, c = 3.8212(4) Å, Z = 2; X = Br: orthorhombic *Pbam*, a = 6.0109(5) Å, b = 12.022(1) Å, c = 4.0230(2) Å, Z = 2).

Keywords: manganese; ammines; chloride; bromide; structure; Raman; ammonia storage; hydrogen storage

1. Introduction

Fossil fuel depletion and societal demands are driving the need for more sustainable fuels. Hydrogen, a plausible high energy density alternative to fossil fuels, must comply with stringent

performance requirements in order to be economically viable and safe for commercial and public use [1]. It may be safely stored in a solid material and subsequently exploited to drive fuel cells, which form the basis of many automotive power systems [2]. The storage of hydrogen in the solid state presents major technical challenges however, with the performance of many candidate materials hampered by poor thermodynamic and/or kinetic H_2 sorption properties. Synthesis, understanding and ultimately improvement of the properties of novel materials for hydrogen storage are critical to the development of sustainable energy stores and delivery systems [3–7].

The storage of hydrogen as ammonia presents an alternative to conventional metal/complex hydride stores. Previous work on ammines, $M(NH_3)_mX_n$, (where M = metal and X = halide; typically $1 \geq m \geq 9$ and $1 \geq n \geq 3$) has highlighted their potential as indirect hydrogen stores [8,9]. However, structural characterization of metal ammines and their decomposition products is required to understand fully the mechanisms by which ammonia release occurs and hence establish where improvements may be made for such systems. Research on metal ammines as solid-state gas stores has recently focused on $Mg(NH_3)_6Cl_2$ [10–13]. This ammine has an exceptional high gravimetric capacity of ammonia and hence hydrogen (51.8 wt% and 9.2 wt% respectively), while the apparent toxicity of the ammonia held within the complex is less than that of alternative fuels such as methanol and gasoline [14]. $Mg(NH_3)_6Cl_2$ releases ammonia in three stages, with the initial release of 4 ammonia equivalents occurring at 350 K, and subsequent single equivalent ammonia releases at 500 K and 620 K. Similarly, the complexation of transition metals with ammonia is well known and transition metal ammines, such as $Fe(NH_3)_nCl_2$ and $Ni(NH_3)_nCl_2$ [15,16], offer flexibility in the design of systems with tunable ammonia release thermodynamics. Such compounds are now at the point of being understood and developed. Hence there is scope for solid state ammonia stores both for ammonia-fed solid oxide fuel cells (SOFCs) at high temperature or via catalytic conversion of ammonia to hydrogen for use in polymer electrolyte membrane (PEM) FCs at lower temperature. Currently commercial liquid/gaseous ammonia is the predominant feed for high temperature systems [17–20], where most research efforts are focused on use of ammonia in SOFCs [21,22].

One ammine system with promising desorption behavior is $Mn(NH_3)Cl_2$ [23]. The relatively high gravimetric capacity of ammonia—and hence potentially hydrogen capacity—in $Mn(NH_3)_6Cl_2$ and also $Mn(NH_3)_6Br_2$ indicates the potential of these materials for development as ammonia and/or hydrogen stores (Table 1).

Table 1. Theoretical gravimetric capacities for manganese halide ammines.

Ammine	NH_3 content/wt%	H_2 content/wt%
$Mn(NH_3)_6Cl_2$	44.83	7.89
$Mn(NH_3)_6Br_2$	32.25	5.74

Olovosson originally proposed that transition metal hexa-ammines should form with cubic K_2PtCl_6-type structures [24]. Almost 30 years later, single crystal X-ray data confirmed this premise for a number of transition metal hexa-ammines synthesized in supercritical ammonia, including $Mn(NH_3)_6Cl_2$ [25]. The unit cell of the ammine, highlighting the arrangement of isolated octahedral $[Mn(NH_3)_6]^{2+}$ complex cations and Cl^- counter anions is shown in Figure 1. The decomposition of $Mn(NH_3)_6Cl_2$ has been studied on two occasions previously and the thermodynamic parameters for

desorption are listed in Table 2 [23,26]. By contrast, little is known regarding the deammoniation profile of $Mn(NH_3)_6Br_2$ and the structures of the lower ammonia adducts of both the chloride and bromide are unknown. We describe here a systematic study of the deammoniation behavior of the manganese chloride and bromide hexa-ammines. By using a combination of powder X-ray diffraction (PXRD) and Raman spectroscopy, we have confirmed the structure of $Mn(NH_3)_6Cl_2$, determined the structure of the hexa-ammmine $Mn(NH_3)_6Br_2$ and the respective diammines $Mn(NH_3)_2Cl(Br)_2$ and verified the decomposition pathway in these systems from the fully ammoniated compounds to the respective dihalides.

Figure 1. K_2PtCl_6-type cubic structure of $Mn(NH_3)_6Cl_2$ [24]. Mn (grey spheres), N (blue spheres), Cl (green spheres).

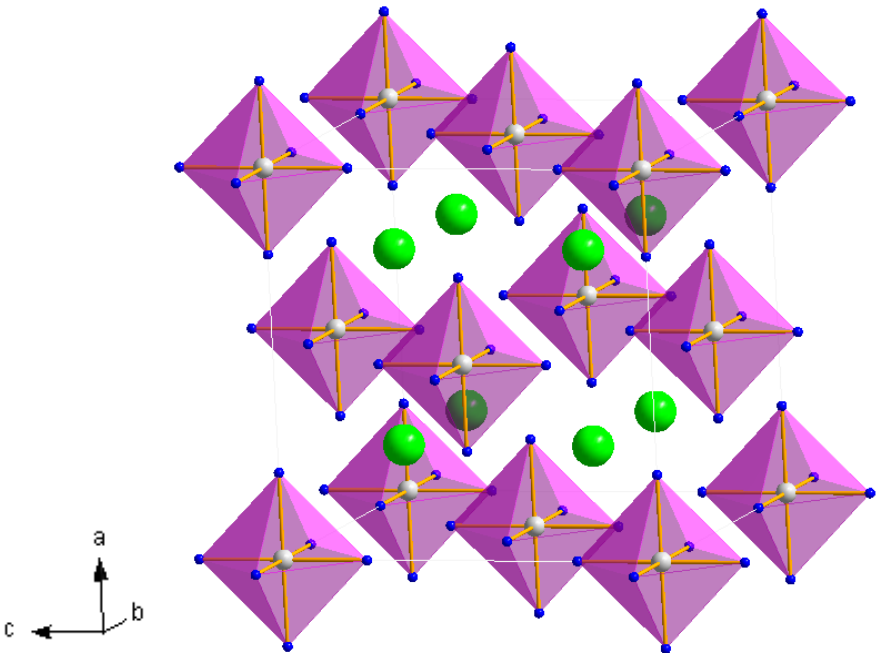

Table 2. Reaction entropy and enthalpy values for the decomposition of manganese halide ammines given by Wentworth *et al.* [26] Values in parenthesis are from the work of Lepinasse and Spinner [27].

	Hexa-ammine → di-ammine		**Di-ammine → mono-ammine**		**Mono-ammine → dihalide**	
	ΔS_{100} †	**ΔH**	**ΔS_{100} †**	**ΔH**	**ΔS_{100} †**	**ΔH**
	(J/K mol)	**(kJ/mol)**	**(J/K mol)**	**(kJ/mol)**	**(J/K mol)**	**(kJ/mol)**
Cl	148.53	47.28 (47.42)	153.55	71.13 (71.02)	153.97	84.10 (84.20)
Br	149.79	53.14	152.30	76.99	154.39	83.68

† Subscript (100) value refers to the vapor pressure, 100 Torr, of ammonia at which ammine equilibria have been characterized at a given temperature for the corresponding complexes. Values listed here are based on experimental data, which established the T_{100} (temperature at which P = 100 torr) and ΔH in order to calculate ΔS_{100} (=$\Delta H/T_{100}$), allowing subsequent data fitting to the Nernst equation [28].

2. Results and Discussion

2.1. Structural Characterization of the Hexa-ammines, $Mn(NH_3)_6X_2$ (X = Cl, Br)

Reaction of $MnCl_2$ and $MnBr_2$ with ammonia gas at room temperature led to white air-sensitive powders of the ammine complexes, **1** and **2** respectively. Raman spectra for **1** and **2** are shown in Figure 2 By comparison with published data for transition metal hexa-ammine complexes, the bands for **1** and **2** could be fully assigned to N–H and Mn–N vibrations (Table 3) [29–33]. Previous IR studies on the $M(NH_3)_6I_2$ (M = Mn, Fe) complexes have suggested that the rotation of ammonia molecules about the M-N axis is possible [34]. From the results presented here we can establish that this is also the case at least for $Mn(NH_3)_6Br_2$ owing to the degenerate (δ_d) band observed in the Raman spectra at 1590 cm^{-1} and also the large H-H bond lengths suggested from XRD refinements (Tables 3–6). Despite the apparent absence of the equivalent δ_d band in the Raman spectrum of **1**, there are sizeable intermolecular distances between neighbouring H atoms in the ammonia molecules (indeed the partially occupied H positions in the model assume dynamic disorder) and no obvious structural reason why rotation should not occur, suggesting that the band is simply too weak in the spectrum of **1** to be observed. This is consistent with the study by Eβmann *et al.* who infer that the rotation of the ammonia molecules about the M-N axis in a number of transition metal ammine chlorides and bromides is free at room temperature [25]. Further, the rotational effects observed for the ammonia molecules in single crystals of $Ni(NY_3)_6X_2$ (Y = H, D and X = Br, I, NO_3, PF_6) as investigated by neutron diffraction are described in more detail by Schiebel *et al*. [35,36].

Table 3. Raman data for $Mn(NH_3)_6X_2$ (X = Cl, Br).

Compound	Raman Shift/cm^{-1}								
	ν_{as} (NH_3)	ν_s (NH_3)	ν_s (NH_3)	δ_d (HNH)	δ_s (HNH)	δ_{as} (HNH)	ρ_r (NH_3)	ν (MN)	δ (MNM)
1	3335	3255	3155	-	1246	1079	644	323	166
2	3321	3243	3149	1590	1239	1076	557	322	150

Table 4. Crystallographic data for hexa-ammines **1** and **2**.

Compound	1	2
Formula	$Mn(NH_3)_6Cl_2$	$Mn(NH_3)_6Br_2$
Crystal System	Cubic	Cubic
Space Group	*Fm*-3*m*	*Fm*-3*m*
***a*/Å**	10.2742(6)	10.528(1)
Volume/Å^3	1084.5(2)	1166.8(4)
Z	4	4
Formula Weight/g	912.120	1267.728
Calculated density, ρ_X/g cm^{-3}	1.397	1.804
No of data	4018	4137
No of parameters	29	36
R_{wp}	0.055	0.073
R_p	0.043	0.058
χ^2	1.101	1.073

Table 5. Atomic parameters for **1** and **2** from Rietveld refinement against PXRD data.

Atom	**$Mn(NH_3)_6Cl_2$ (1)**	**$Mn(NH_3)_6Br_2$ (2)**
Mn, 4*a* (0,0,0)		
$U_{iso} \times 100/Å^2$	5.7(4)	3.3(3)
X, 8*c* (¼, ¼, ¼)		
$U_{iso} \times 100/Å^2$	5.4(4)	5.0(2)
N, 24*e* (*x*, 0, 0)		
X	0.218(1)	0.220(2)
$U_{iso} \times 100/Å^2$	6.0(7)	6.3(9)
H, 96*k* (*x*, *x*, *z*)		
X	0.066(4)	0.055(3)
Z	0.265(3)	0.248(5)
$U_{iso} \times 100/Å^2$	2.5	2.5
Occupancy	0.75	0.75

Figure 2. Raman spectra for **1**; (**a**) 50–1500 cm^{-1}, (**b**) 1500–3600 cm^{-1}, and **2** (**c**) 50–3600 cm^{-1}.

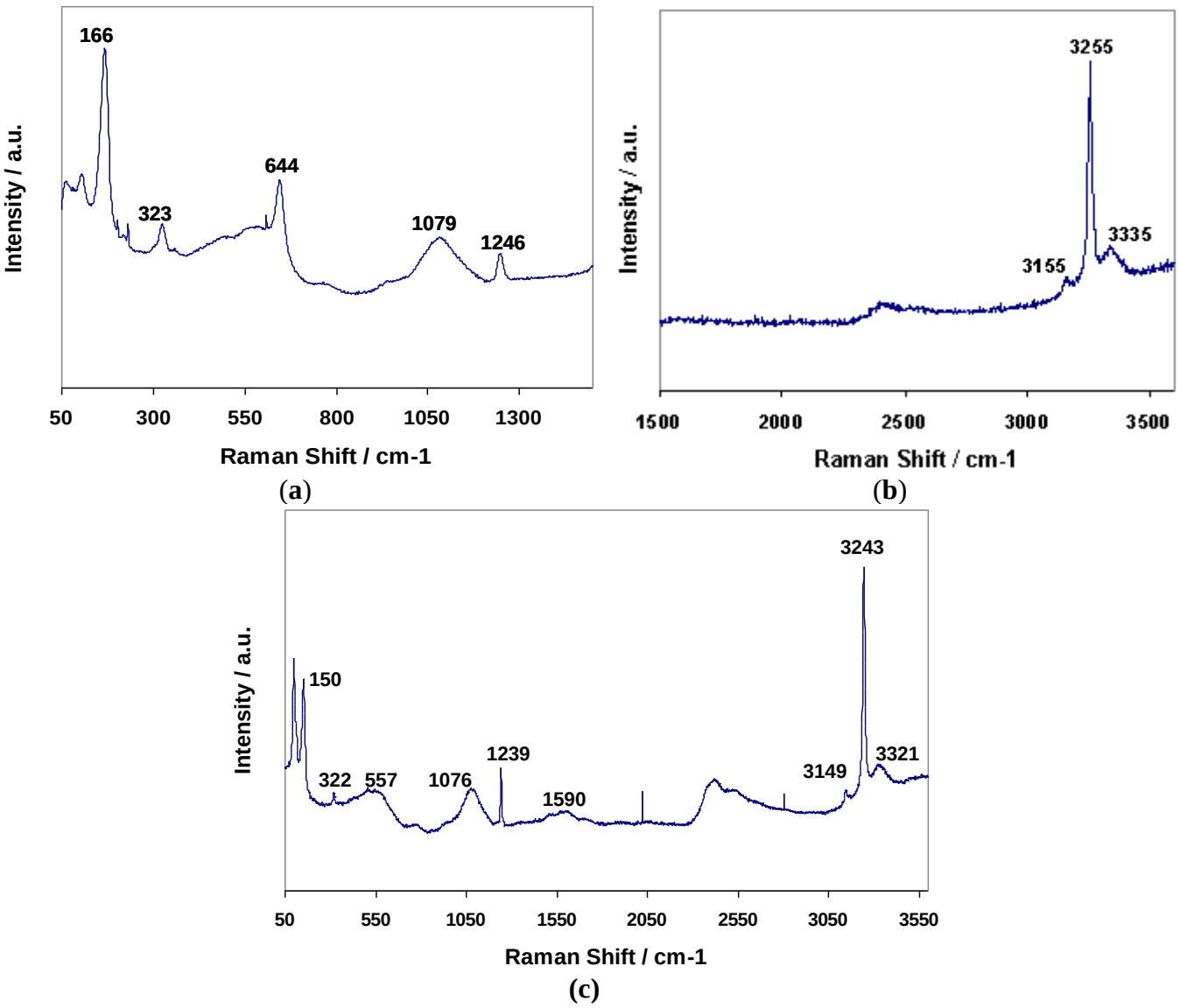

Table 6. Interatomic distances and angles for **1** and **2**.

Distance or angle/Å or °	**$Mn(NH_3)_6Cl_2$ (1)**	**$Mn(NH_3)_6Br_2$ (2)**
8 × Mn–X/Å	4.44886(19)	4.5586(4)
6 × Mn–N/Å	2.239(15)	2.313(18)
N–H/Å	1.07(5) 3.210(26) × 6 4.05(4) × 4	0.88(6) 3.183(34) × 5 3.94(5) × 2 4.99(4) × 3
H1–H1/Å	2.89(8) × 2 3.97(4) × 2 4.19(5) × 2 4.81(7) × 2 4.83(7)	2.86(8) × 2 3.78(8) × 2 3.95(8) × 2 4.51(10) × 2
X–Mn–X/ °	70.529(2) × 2 70.529(4) 109.471(4) × 3 179.972(1)	109.471(5) × 3 70.529(5) × 2 180.000

Initial search-matching procedures for the PXRD powder pattern of **1** revealed a match with that of the corresponding Mg analogue (PDF card No: 01-075-6756) and the pattern could be indexed to a cubic cell with a = 10.442 Å [9]. Although there is no refined crystal structure for $Mn(NH_3)_6Br_2$, Watt and Manhas reported XRD data (and elemental analysis) for the hexa-ammine formed by the reaction of $MnBr_2$ with liquid ammonia [37]. The PXRD data obtained for **2** matched well with the pattern of $Fe(NH_3)_6Br_2$ (PDF card No: 01-085-2095), which was generated using the Powdercell software package from single crystal structural data, and could thus be indexed to a cubic unit cell with a = 10.249 Å [25,38]. From the observed reflections, it was thus deduced that $Mn(NH_3)_6Br_2$ and $Mn(NH_3)_6Cl_2$ were isostructural. Subsequent Rietveld refinements for **1** and **2** were performed taking the previous single crystal X-ray structure of $Mn(NH_3)_6Cl_2$ and isostructural $Fe(NH_3)_6Br_2$ as the respective starting models [25]. The refinements of **1** and **2** were performed following an identical strategy in which the background coefficients (GSAS Function 8, a reciprocal interpolation function), scale factor and the unit cell parameters were varied in the initial cycles. The atomic parameters, peak profile parameters and isotropic displacement parameters (for non-hydrogen atoms) were varied subsequently. Modeling of the peak shapes used function 2, the Thompson-Cox-Hastings pseudo-Voigt function. The final crystallographic results for **1** and **2** are presented in Table 4, atomic parameters in Table 5 and interatomic distances angles in Table 6. Profile plots for the refinements are shown in Figures 3,4.

Figure 3. Rietveld refinement profile for **1** from PXRD data. Crosses indicate the observed data, the upper continuous line shows the calculated profile and the lower continuous line the difference profile. Tick marks show reflection positions for cubic $Mn(NH_3)_6Cl_2$.

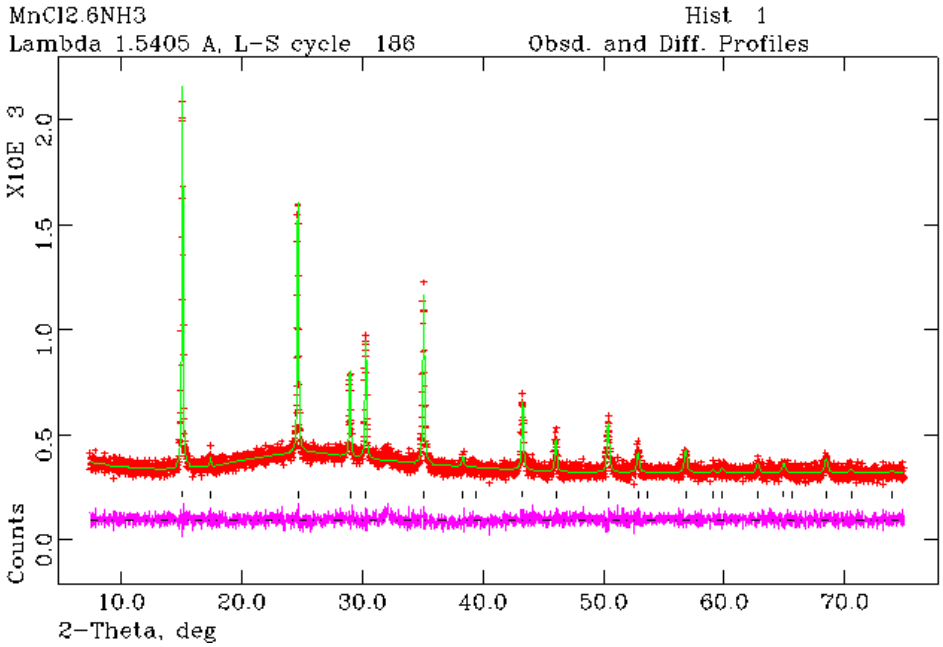

Figure 4. Rietveld refinement profile for **2** from PXRD data. Crosses indicate the observed data, the upper continuous line shows the calculated profile and the lower continuous line the difference profile. Tick marks show reflection positions for cubic $Mn(NH_3)_6Br_2$.

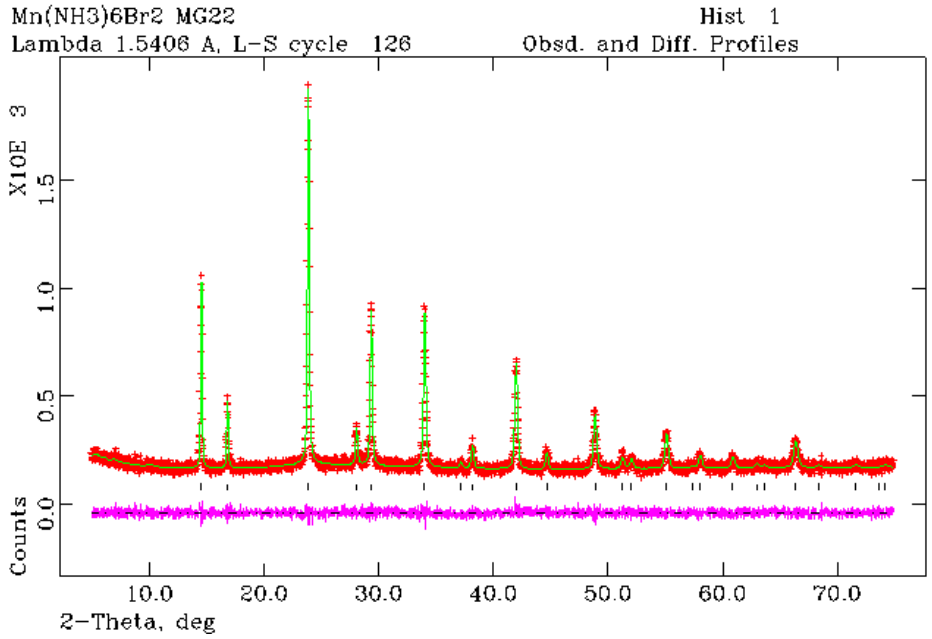

Structure refinement against PXRD data confirmed that $Mn(NH_3)_6Cl_2$ (**1**) forms with the cubic $K_2[PtCl_6]$-type structure as previously reported from single crystal X-ray analysis [24]. Rietveld refinement has also established for the first time that $Mn(NH_3)_6Br_2$ also crystallizes with the $K_2[PtCl_6]$-type structure and is thus isostructural with the chloride and $Fe(NH_3)_6Br_2$ (Figure 4) [25]. The hexa-ammine structures can be considered to be composed of a FCC lattice of isolated octahedral

complex ammoniate cations, *i.e.*, $[Mn(NH_3)_6]^{2+}$, with halide anions, *X* (*X* = Cl^-, Br^-), occupying the tetrahedral interstices of the unit cell in a distorted close-packed cubic configuration (Figure 1) [39]. Although these $[Mn(NH_3)_6]^{2+}$ octahedra are effectively isolated, Sørensen *et al.* have evoked the concept of weakly bound—$[Mn(NH_3)_6]$–X—"chains" in rationalizing the ammonia sorption mechanism [23]. These chains are thus composed of metal octahedra connected along the chain length via the interceding halide anions. Alternatively, the cubic hexa-ammine structure could be viewed as a simple cubic lattice of halide anions with nitrogen occupying the faces of each halide cube and manganese located in the body centers of alternate halide cubes.

We observe that the cubic structure expands as a result of the replacement of Cl^- by Br^- as would be anticipated from ionic radii arguments [40,41]. Previously reported structural models of the hexa-ammines have defined partially occupied hydrogen positions (96 *k* sites that are 75% occupied) reflecting the dynamic disorder of the ammonia ligands in the octahedral cations. Although it would not be expected that powder X-ray diffraction methods could resolve the positions and disorder of the hydrogen with any great accuracy, we were tentatively able to vary the hydrogen coordinates and achieve stable, convergent refinements with reasonable N–H bond distances. The Mn–N distances in the complex cations are similar to those observed for other transition metals in equivalent ammoniates and the bond length increases slightly from chloride to bromide [25].

2.2. Deammoniation of the Hexa-ammines by TPD

The TGA results collected to 773 K for **1** and **2** (Figures 5, 6, Table 7) show a 3-stage mass loss in each case which, by simultaneous MS analysis of the gases released, is associated solely with the loss of ammonia. The DTA data indicate four distinct endothermic events with minima at 379.3 K, 490.6 K, 556.7 K and 574.5 K respectively for **1**, and three distinct endothermic events at 407.5 K, 516.6 K and 565.2 K for **2** that correlate to each mass loss for both complexes. Careful isolation of the di- and mono-ammoniated compounds using TG-DTA has been possible by ceasing the heating process at the appropriate stage of decomposition. For the chloride complex, TGA analysis to 398 K and 498 K allowed isolation of the di- and mono-ammoniated decomposition products respectively. Slightly higher temperatures were used to isolate the di- and mono-ammoniates for the bromide; 423 K and 523 K respectively. The increase in deammoniation temperatures from the **1** to **2** is unsurprising upon consideration of the respective enthalpies for the ammines in Table 2.

Table 7. De-ammoniation parameters of $Mn(NH_3)_6Cl_2$ ($Mn(NH_3)_6Br_2$).

Step	Expected number of equivalent ammonia molecules lost	Expected weight loss/%	Observed weight loss/%	Onset temperature of deammoniation, T_i/K	Final temperature of deammoniation, T_f/K
1	4	29.8 (21.5)	26.9 (19.8)	300.8 (298.5)	401.1 (428.6)
2	1	7.5 (5.4)	7.8 (5.5)	410.3 (449.6)	504.0 (528.4)
3	1	7.5 (5.4)	7.2 (5.5)	504.0 (528.4)	590.1 (584.5)
Total	6	44.8 (32.3)	41.8 (30.8)	-	-

Figure 5. (**a**) TG-DTA data, and (**b**) corresponding MS data for the thermal decomposition of $Mn(NH_3)_6Cl_2$.

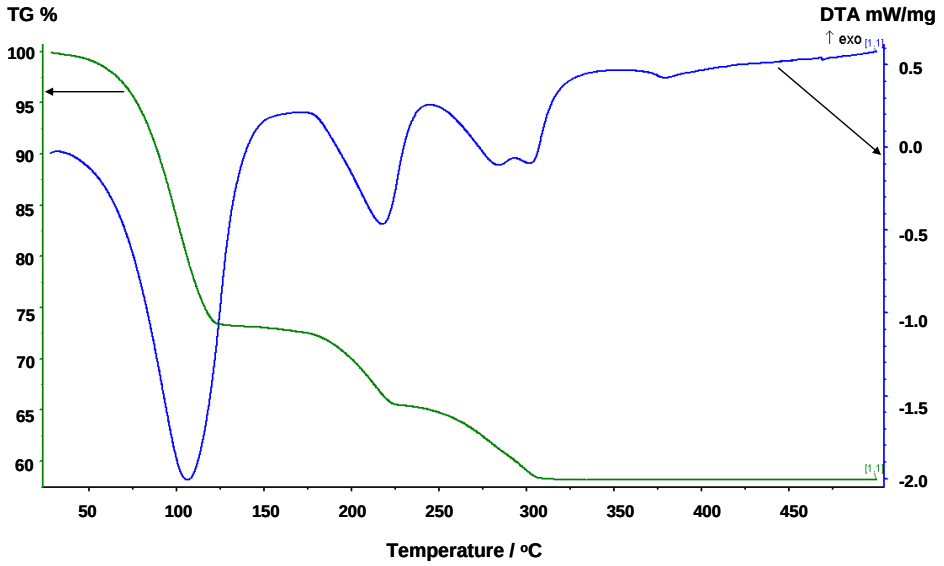

(**a**)

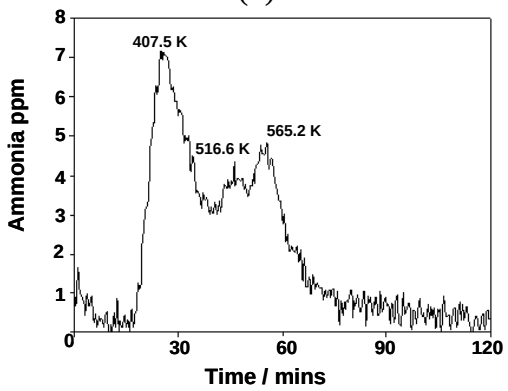

(**b**)

Figure 6. (**a**) TG-DTA data, and (**b**) corresponding MS data for the thermal decomposition of $Mn(NH_3)_6Br_2$.

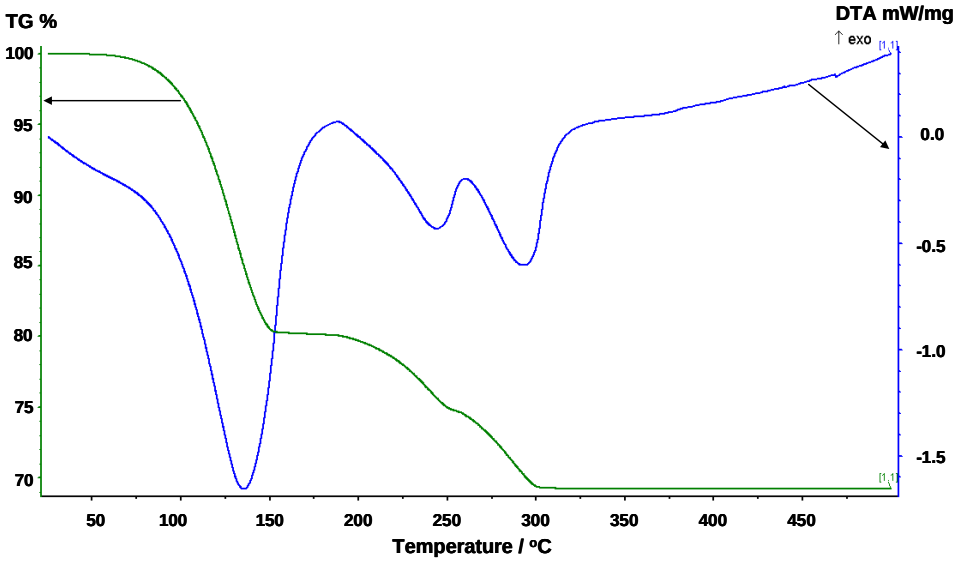

(**a**)

Figure 6. *Cont.*

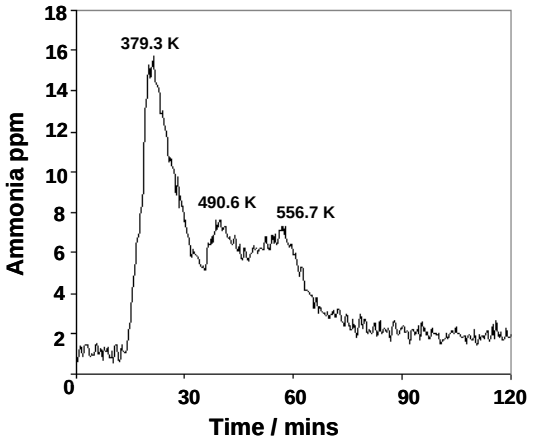

(**b**)

Reaction Scheme 1 hence describes the anticipated route by which the chloride and bromide ammoniates release ammonia in accordance with the TPD data observed in this study. These are comparable with data observed in literature for various dichloride ammines [9]. The TGA profile in Figure 6 suggests that weight loss for **1** occurs almost immediately (marginally above room temperature) and in contrast to previous work, ammonia desorption is complete below 600 K. The bromide, **2**, begins to desorb ammonia at a higher temperature than the chloride commensurate with its higher desorption enthalpy (Table 2), but this onset still lies below 373 K.

$$Mn(NH_3)_6X_2 \rightarrow Mn(NH_3)_2X_2 + 4\,NH_3 \rightarrow Mn(NH_3)X_2 + 5\,NH_3 \rightarrow MnX_2 + 6\,NH_3 \qquad (1)$$

Although ostensibly both halides exhibit a three-step loss of ammonia with increasing temperature, it is evident from close examination of the chloride DTA profile (Figure 5) that the transformation from the presumed mono-ammine to the deammoniated chloride, $MnCl_2$, appears to progress through two closely spaced (almost overlapping) thermal events. Indeed, a change in the slope of the TGA profile at the same temperature as the double minimum in the DTA trace (556.7 and 574.5 K) would also suggest that the loss of the final ammonia molecule is not a stoichiometric process from mono-ammine to $MnCl_2$. This TG-DTA profile is in agreement with two (or more) gas releases from nominal $Mn(NH_3)Cl_2$ measured by Sørensen *et al.*, although the equivalent desorption in their study appeared to occur at a temperature *ca*. 80 K above that seen herein [9]. By contrast, the temperature range over which the dibromide deammoniates is narrower, which results in the successive deammoniation steps being less widely spaced (in temperature and time) and, for example a stability domain for the nominal mono-ammine of only several *K*. Although the final desorption step has not yet been resolved into more than one event in either the DTA or TGA traces, the asymmetry of the DTA peak and the fluctuations in slope of the TGA trace would suggest an analogous non-stoichiometric decomposition from mono-ammine to dihalide to that observed for **1**. A mechanism for ammonia absorption/desorption for $M(NH_3)_nCl_2$ (*M* = Mg, Mn, Ni) ammines was proposed by Sørensen *et al.* using DFT calculations. This model indicated that ammonia molecules could enter and leave the bulk interface via the zipping/unzipping of the loosely-bound "chains" of octahedral ML_6 groups (where *L* could be either NH_3 and/or Cl depending on *n*) to allow conservation of the metal coordination geometry independent of n. This model necessarily also involves structural rearrangement in the bulk

after each successive sorption step. In the later deammoniation steps, for example, it would be necessary not only for Cl to substitute for NH_3 in each ML_6 octahedron, but also for the resulting octahedra to condense and form edge sharing chains. The structures of the lower Mn ammines are discussed in more detail below, but the non-stoichiometric decomposition from mono-ammine to dihalide observed above could be rationalized in the intermediate loss of one NH_3 unit for every two Mn centers in the edge-sharing octahedral clusters in $Mn(NH_3)X_2$ and a process as described in Scheme 2:

$$2\,Mn(NH_3)X_2 \rightarrow 2\,Mn(NH_3)_{0.5}X_2 + NH_3 \rightarrow 2\,MnX_2 + 2\,NH_3 \quad (2)$$

2.3. Structural Characterization of the Lower Ammoniates

Decomposition of **1** and **2** to 398 K and 423 K respectively in the TG-DTA experiments led to small samples (*ca*. 50 mg) of air-sensitive, light pink and light orange/brown powders (**3** and **4**) respectively. Decomposition of **1** and **2** conducted to higher temperatures, 498 and 523 K respectively, led to air-sensitive, pink and light orange/brown powders to give the nominal mono-ammoniated complexes, **5** and **6** respectively. After weight losses were complete for both systems a blackened solid mass (**7**) and an orange/brown powder (**8**) respectively were the result. Raman spectra for **3** and **4** are shown in Figures 7a,b respectively, and assignments are given in Table 8. The bands for **3** and **4** have been assigned to N–H and Mn–N vibrations based on the premise that similar bonding modes exist in both the hexa- and di-ammines. The presence of the weak degenerate δ_d band at 1599 cm^{-1} in **4** would suggest that there is similar dynamic disorder (rotation) of NH_3 groups in the diammines to that observed in the hexammines (and again this band is observable in the bromide but not the chloride).

Figure 7. Raman data for (**a**) $Mn(NH_3)_2Cl_2$ and (**b**) $Mn(NH_3)_2Br_2$.

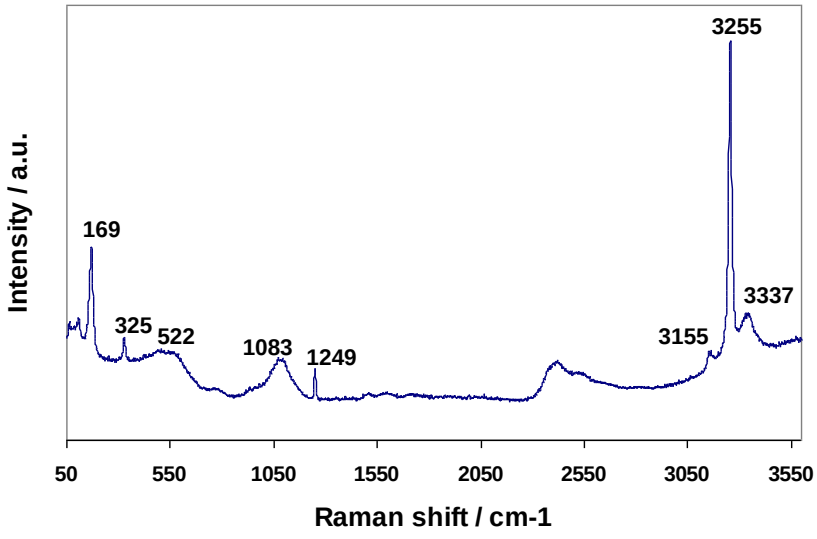

(**a**)

Figure 7. *Cont.*

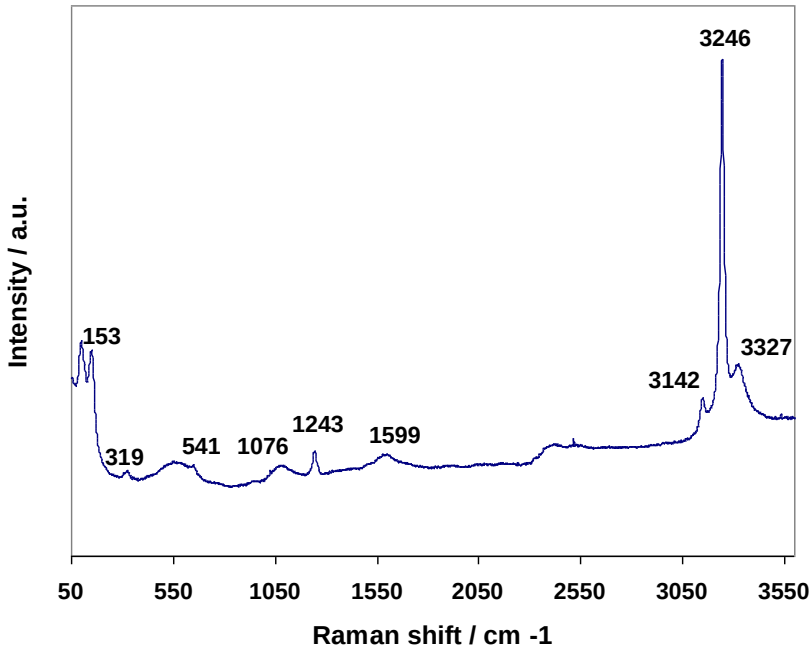

(**b**)

Table 8. Raman data for $Mn(NH_3)_2X_2$ (X = Cl, Br).

Compound	Raman Shift/cm^{-1}								
	ν_{as} (NH_3)	ν_s (NH_3)	ν_s (NH_3)	δ_d (HNH)	δ_s (HNH)	δ_{as} (HNH)	ρ_r (NH_3)	ν (MN)	δ (MNM)
3	3337	3255	3155	-	1249	1083	522	325	169
4	3327	3246	3142	1599	1243	1076	541	319	153

Initial search-matching procedures for the PXRD powder pattern of **3** revealed a match with the Mg analogue (PDF card No: 01-073-4070) and the pattern could be indexed to an orthorhombic unit cell with a = 8.180 Å, b = 8.200 Å, c = 3.750 Å [41]. From the observed reflections, it was deduced that **3** was isostructural with $Fe(NH_3)_2Cl_2$ and $Mg(NH_3)_2Cl_2$ and matched well to a powder pattern generated using Powdercell in which Mn was placed on the Fe positions of the orthorhombic *Cmmm* $Fe(NH_3)_2Cl_2$ structure [15]. Inspection of patterns for **4** revealed a match with that of the corresponding Mg analogue (PDF card No: 01-089-6789) [38, 41]. The pattern for **4** could be indexed to an orthorhombic unit cell with a = 5.944 Å, b = 11.876 Å, c = 3.983 Å and it was apparent that **4** was isostructural with $Fe(NH_3)_2Br_2$ and $Mg(NH_3)_2Br_2$ (orthorhombic *Pbam*) [16,38,41].

Subsequent Rietveld refinements for **3** and **4** were performed taking the previous single crystal X-ray structures of the relevant isostructural iron ammines as the respective starting models [16]. The refinements were conducted using PXRD data collected from the di-ammine products from the TG-DTA experiments, *i.e.*, **3** and **4**, which were isolated by heating **1** and **2** to 398 K and 423 K respectively. The refinements of **3** and **4** were performed following a similar sequence in which the background coefficients (GSAS Function 8, a reciprocal interpolation function), scale factor and the unit cell parameters were varied in the initial cycles. The peak profile parameters, atomic parameters including isotropic displacement parameters (for non-hydrogen atoms) were varied subsequently.

Modeling of the peak shapes was performed using the Thompson-Cox-Hastings pseudo-Voigt function (function 2 in GSAS). It was not possible in the refinements of either **3** or **4** to refine the positions or displacement parameters of the hydrogen atoms, so these were fixed at values from the literature models of the equivalent iron compounds [16]. The final crystallographic results for **3** and **4** are presented in Table 9, atomic parameters in Table 10 and interatomic distances and angles in Table 11. (STA data for the isolation of the di-ammines and profile plots for the refinements can be found in the supplementary material).

Table 9. Crystallographic data from Rietveld refinement of PXRD data for di-ammines, **3** and **4**.

Compound	**3**	**4**
Formula	$Mn(NH_3)_2Cl_2$	$Mn(NH_3)_2Br_2$
Crystal System	Orthorhombic	Orthorhombic
Space Group	*Cmmm*	*Pbam*
***a*/Å**	8.1991(9)	6.0109(5)
***b*/Å**	8.2498(7)	12.022(1)
***c*/Å**	3.8212(4)	4.0230(2)
Volume/Å^3	258.47(7)	290.72(4)
Z	2	2
Formula Weight/g	319.812	497.616
Calculated density, ρ_X/g cm^{-3}	2.055	2.842
No of data	3290	3410
No of parameters	34	36
R_{wp}	0.034	0.065
R_p	0.025	0.048
χ^2	2.182	8.303

Table 10. Atomic parameters for **3** and **4** from Rietveld refinement against PXRD data.

Compound	**$Mn(NH_3)_2Cl_2$ (3)**	**$Mn(NH_3)_2Br_2$ (4)**
Mn	*2a* (0,0,0)	*2a* (0,0,0)
U_{iso}	1.0(2)	2.0(2)
X	*4h* (*x*, 0, ½)	*4h* (*x*, *y*, ½)
X	0.2244(6)	0.2439(9)
Y	0	0.3904(2)
U_{iso}	0.4(3)	1.65(9)
N	*4i* (0, *y*, 0)	*4g* (*x*, *y*, 0)
X	0	0.193(3)
Y	0.270(2)	0.140(2)
U_{iso}	2.50	2.50
H(1)	16*r* (*x*, *y*, *z*)	8*i* (*x*, *y*, *z*)
X	0.045	0.355
Y	0.312	0.109
Z	0.158	0.143
U_{iso}	2.50	2.50
Occupancy	0.75	0.75
H(2)		8*i* (*x*, *y*, *z*)
X		0.220
Y		0.177
Z		0.143
U_{iso}		2.50
Occupancy		0.75

Table 11. Interatomic distances and angles for **3** and **4**.

Distance or angle/Å or °	$Mn(NH_3)_2Cl_2$ (3)	$Mn(NH_3)_2Br_2$ (4)
Mn–N/Å	2.231(16) ×2	2.046(30) ×2
Mn–X/Å	2.653(4) ×4	2.855(3) ×4
N–H(1)/Å	0.786(7) ×4	1.190(13) ×2
N–H(2)/Å		0.743(19) ×2
X–H/Å	2.57(5) ×4	2.743(5) ×2
H(1)–H(1)/Å	0.72(9) 0.93(6) 0.58(9)	1.151(1)
H(1)–H(2)/Å		1.152(1) 1.628(1)
H(2)–H(2)/Å		1.151(1)
X–Mn–X/ °	87.85(16) 92.15(16) 179.966(1)	89.57(13) 90.43(13) 179.980(1)

The unit cell parameters of **3** are slightly larger than those in both the isostructural magnesium and iron chloride ammines as would be expected by comparison of the respective ionic radii of high spin Mn^{2+} *vs.* Mg^{2+} and high spin Fe^{2+} (and as is also the case for the respective hexa-ammines) [37,38,40,41]. A representation of the structure of **3** is given in Figure 8. The structure is composed of edge sharing $Mn(NH_3)_2Cl_4$ octahedra (which can be termed as $^{1}_{\infty}[MnCl_{4/2}(NH_3)_2]$ chains in which the trans-NH_3 groups are thus terminal and the halide groups are bridging) which propagate parallel to the [001] direction. The chains are effectively aligned parallel in the (110) plane throughout the structure with each chain translated by half the [001] face diagonal with respect to its nearest neighbour. Leineweber *et al* have also rationalised the orthorhombic structure in terms of CsCl-type motifs and described isostructural $Mg(NH_3)_2Cl_2$ as a brick-like arrangement of double CsCl units in the *ab* plane [38,41]. The Mn–N bond length in **3** is broadly similar to those in the hexa-ammmines, **1** and **2**, and close to those observed in the equivalent magnesium and iron compounds [16,38,41].

Figure 8. Crystal structure of **3**, $Mn(NH_3)_2Cl_2$; Mn (white sphere), Cl (green spheres), N (blue spheres) [38,41].

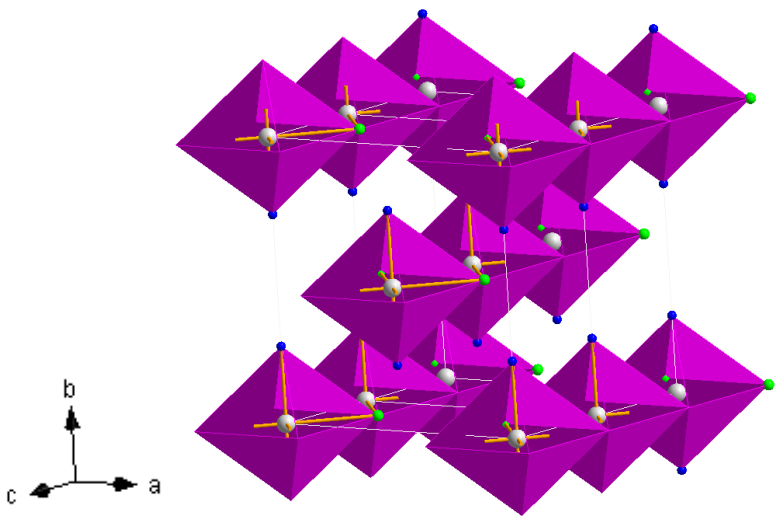

4 is isostructural with $Fe(NH_3)_2Br_2$ and $Mg(NH_3)_2Br_2$ (Figure 9) [16,38,41]. As with **3**, the unit cell of **4** is larger than the Fe and Mg analogues. Similar to **3**, **4** is composed of $^1_\infty[MnX_{4/2}(NH_3)_2]$ chains (where Br replaces Cl as X). The key difference in the structures of **3** and **4** lies in the relative arrangement of these edge sharing octahedral chains. As Bremm and Meyer point out, the packing of the chains in the *Pbam* structures is hexagonal as opposed to the tetragonal sequence in the *Cmmm* compounds [16]. Hence, successive rows of edge-sharing octahedra running parallel to the [110] direction are rotated by 90 °. Following the double CsCl unit notation used by Leineweber *et al*, the units are arranged in a herringbone pattern in the *ab* plane in the bromide (as opposed to the brick-like arrangement in the chloride). Mn–X distances are longer in **4** than **3** as would be expected on coordination of the metal to the larger halides [37,40]. The Mn–N distance in **4** is shorter however and comparable to that observed in $Fe(NH_3)_2Cl_2$. Inevitably from the mismatch in Mn–N and Mn–X bond lengths in both **3** and **4** the $MnX_4(NH_3)_2$ octahedra are axially compressed in both compounds. We are unable to draw any firm conclusions regarding the positions or dynamics of the hydrogens from our relatively limited models from PXRD. The $Mg(ND_3)_2X_2$ compounds have been studied by neutron diffraction to resolve such issues and a similar approach would be required in the Mn–NH_3–*X* systems to understand the relationships of NH_3 rotational disorder with halide and temperature [42].

Figure 9. Crystal structure of **4**, $Mn(NH_3)_2Br_2$; Mn (white sphere), Br (yellow spheres), N (blue spheres) [38,41].

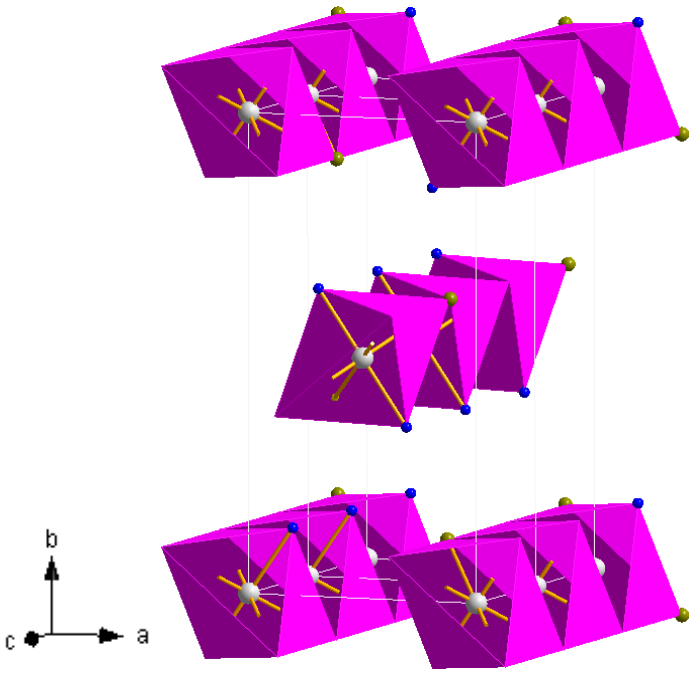

Further de-ammoniation of **1** and **2** to yield the anticipated mono-ammoniated complexes **5** and **6** was performed although isolation of these phases is yet to be achieved owing to the apparent narrow stability range (prior to further desorption). In the available literature, among the transition metal ammines only the $Fe(NH_3)Cl_2$ and $Ni(NH_3)X_2$ (*X* = Cl, Br) have been crystallographically characterized giving hexagonal $P6_3/mmc$ and monoclinic *I*2/*m* structures for the Fe and Ni compounds respectively [16,43]. Further heating of **1** and **2** gave rise to **7** and **8** which were amorphous by PXRD. Raman spectra for **7** and **8** showed no notable features over the measurement range and none of the

bands that were present in **1**–**4** from which one could infer that deammoniation was complete as suggested by the thermogravimetric data.

3. Experimental Section

$MnCl_2$ (Alfa Aesar, anhydrous, 97%) and $MgBr_2$ (Sigma Aldrich, anhydrous, 98%) powders were prepared for ammoniation in an N_2-filled recirculating glovebox (Saffron Scientific; 1 ppm H_2O, 1 ppm O_2). Each halide was weighed and contained in a silica reaction tube fitted with a septum cap and parafilm prior to removal from the glovebox. In a fume hood, ammonia (BOC, anhydrous ammonia gas, 99.98%) was flowed over the transition metal halides at room temperature for 16 h, utilizing a water trap on the exhaust flow. The resultant products (**1** and **2**) were collected in the glovebox and prepared for the appropriate characterization methods below.

Room temperature powder X-ray diffraction (PXRD) experiments were conducted with a PANalytical XPERT Pro MPD diffractometer in Bragg-Brentano reflection geometry (Cu Kα1 radiation) using a bespoke air sensitive sample holder [44]. Diffraction data for phase identification were typically collected for $5\,^\circ \leq 2\theta \leq 85\,^\circ$ with a $0.017\,^\circ$ step size with scan times of from 1–12 h. Diffraction data were compared to patterns in the ICDD (JCPDS) powder diffraction file (PDF) using the PANalytical High Score Plus software package. Additional data for the structure refinement of selected samples were collected over longer scan times (12 h; $5\,^\circ \leq 2\theta \leq 85\,^\circ$ with a step size of $0.017\,^\circ$). All data were indexed where possible using the CELREF software package and refined by least squares fitting [45]. Structure refinements were performed using the Rietveld method via GSAS and EXPGUI software [46,47].

Temperature programmed desorption, via thermogravimetric-differential thermal analysis-mass spectrometry (TG-DTA-MS; Netzsch STA 409 and Hiden Analytical HPR20 using Ar carrier gas) was conducted in an Ar-filled recirculating glovebox (MBraun UniLab; <0.1 ppm H_2O, 0.1 ppm O_2). Using alumina sample pans, the hexa-ammine samples were initially heated to 773 K under a flow of Ar gas at a rate of 5 K min^{-1} to fully de-ammoniate the sample. In initial experiments, MS data were collected up to 200 amu but in later runs only data at values for argon, ammonia, water, nitrogen and hydrogen were collected, given the absence of any other detectable species. Finally, the hexa-ammines were heated again to lower temperatures as appropriate to partially de-ammoniate them and to allow isolation of the decomposition products. Evolved gas analysis by simultaneous mass spectrometry using a Faraday cup detector was employed to provide definitive evidence of ammonia loss during TGA analysis.

Room temperature Raman spectroscopy (Horiba LabRam HR confocal microscope, 532.17 nm green laser, 100 μm aperture, 600 groves/mm grating, Synapse CCD) was used to identify the Raman active bands in the ammines, and hence confirm the vibrational bonding modes occurring in the fully and partially ammoniated complexes. The samples were held in sealed glass capillaries to prevent exposure to air/moisture.

4. Conclusions

$MnCl_2$ and $MnBr_2$ uptake ammonia readily at room temperature to form the respective hexa-ammoniate adducts. $Mn(NH_3)_6Cl_2$ and $Mn(NH_3)_6Br_2$ release near-theoretical equivalents of ammonia in a three stage release process as evidenced by TG-DTA-MS. 4, 1 and 1 equivalents respectively of ammonia are lost by both the chloride and bromide. Generally each respective release occurs at a higher temperature in the bromide system although both hexa-ammines appear to begin losing ammonia under ambient conditions. The hexa-ammine complexes, $Mn(NH_3)_6Cl_2$ and $Mn(NH_3)_6Br_2$, form with the $K_2[PtCl_6]$-type structure, with Raman data consistent with compounds containing NH_3 and are comparable to those in related magnesium and iron ammoniates. The product of the first de-ammoniation steps in each system is confirmed as the diammines $Mn(NH_3)_2Cl_2$ and $Mn(NH_3)_2Br_2$ respectively, which are isostructural with the corresponding Mg and Fe chloride and bromide compounds. Further ammonia loss events would suggest decomposition first to the respective monoamines and finally to the deammoniated dihalides.

Acknowledgments

DHG thanks the EPSRC for funding under grants EP/E040071/1 and EP/I022570/1 and the EPSRC, the Materials KTN and EADS Innovation Works for a CASE studentship for HR.

References

1. DOE Technical Plan—Storage (2011 Interim Update). Available online: http://www1.eere.energy.gov/hydrogenandfuelcells/mypp/pdfs/storage.pdf (accessed on 20 February 2012).
2. Sørensen, B. *Hydrogen and Fuel Cells: Emerging Technologies and Applications*, 2nd ed.; Academic Press: New York, NY, USA, 2005.
3. Mandal, T.K.; Gregory, D.H. Hydrogen Storage Materials: present scenarios and future directions. *Ann. Rep. Prog. Chem. Sect. A* **2009**, *105*, 21–54.
4. Mandal, T.K.; Gregory, D.H. Hydrogen: a future energy vector for sustainable development. *J. Mech. Eng. Sci.* **2010**, *224*, 539–558.
5. Orimo, S.; Nakamori, Y.; Eliseo, J.R.; Züttel, A.; Jensen, C.M. Complex Hydrides for Hydrogen Storage. *Chem. Rev*. **2007**, *107*, 4111–4132.
6. Grochala, W.; Edwards, P.P. Thermal Decomposition of the Non-Interstitial Hydrides for the Storage and Production of Hydrogen. *Chem. Rev.* **2004**, *104*, 1238–1315.
7. Schlapbach, L.; Züttel, A. Hydrogen-storage materials for mobile applications. *Nature* **2001**, *414*, 353–358.
8. Christensen, C.H.; Sørensen, R.Z.; Johannessen, T.; Quaade, U.J.; Honkala, K.; Elmøe, T.D.; Køhler, R.; Nørskov, J.K. Metal ammine complexes for hydrogen storage. *J. Mater. Chem.* **2005**, *15*, 4106–4108.
9. Sørensen, R.Z.; Hummelshøj, J.S.; Klerke, A.; Reves, J.B.; Vegge, T.; Nørskov, J.K.; Christensen, C.H. Indirect, Reversible High-Density Hydrogen Storage in Compact Metal Ammine Salts. *J. Am. Chem. Soc*. **2008**, *130*, 8660–8668.

10. Hwang, I.-C.; Drews, T.; Seppelt, K. $Mg(NH_3)_6Hg_{22}$, a Mercury Intercalation Compound. *J. Am. Chem. Soc.* **2000**, *122*, 8486–8489.
11. Jacobsen, H.S.; Hansen, H.A.; Andreasen, J.W.; Shi, Q.; Andreasen, A.; Feidenhans'l, R.; Nielsen, M.M.; Ståhl, K.; Vegge, T. Nanoscale structural characteriszation of $Mg(NH_3)_6Cl_2$ during NH_3 desorption: An *in situ* small angle X-ray scattering study. *Chem. Phys. Lett.* **2007**, *441*, 255–260.
12. Tsubota, M.; Hino, S.; Fujii, H.; Oomatsu, C.; Yamana, M.; Ichikawa, T.; Kojima, Y. Reaction between magnesium ammine complex compound and lithium hydride. *Int. J. Hydrogen Energy* **2010**, *35*, 2058–2062.
13. Tekin, A.; Hummelshøj, J.S.; Jacobsen, H.S.; Sveinbjørnsson, D.; Blanchard, D.; Nørskova, J.K.; Vegge, T. Ammonia dynamics in magnesium ammine from DFT and neutron scattering. *Energy Environ. Sci.* **2010**, *3*, 448–456.
14. Klerke, A.; Christensen, C.H.; Nørskov, J.K.; Vegge, T. Ammonia for hydrogen storage: challenges and opportunities. *J. Mater. Chem.* **2008**, *18*, 2304–2310.
15. Leineweber, A.; Jacobs, H. Preparation and Crystal Structures of $Ni(NH_3)_2Cl_2$, and of Two Modifications of $Ni(NH_3)_2Br_2$ and $Ni(NH_3)_2I_2$ *J. Solid State Chem.* **2000**, *152*, 381–387.
16. Bremm, S.; Meyer, G. Reactivity of Ammonium Halides: Action of Ammonium Chloride and Bromide on Iron and Iron(III) Chloride and Bromide. *Z. Anorg. Allg. Chem.* **2003**, *629*, 1875–1880.
17. Lan, R.; Irvine, J.T.S.; Tao, S. Ammonia and related chemical as potential indirect hydrogen storage materials. *Int. J. Hydrogen Energy* **2012**, *37*, 1482–1494.
18. Fuerte, A.; Valenzuela, R.X.; Escudero, M.J.; Daza, L. Ammonia as efficient fuel for SOFC. *J. Power Sources* **2009**, *192*, 170–174.
19. Farhad, S.; Hamdullahpur, F. Conceptual design of a novel ammonia-fuelled portable solid oxide fuel cell system. *J. Power Sources* **2010**, *195*, 3084–3090.
20. Ishak, F.; Dincer, I.; Zamfirescu, C. Thermodynamic analysis of ammonia-fed solid oxide fuel cells. *J. Power Sources* **2012**, *202*, 157–165.
21. Ma, S.; Wang, J.; Yan, Z.; Dai, W.; Lu, B. Thermodynamic analysis of a new combined cooling, heat and power system driven by solid oxide fuel cell based on ammonia-water mixture. *J. Power Sources* **2011**, *196*, 8463–8471.
22. Baniasadi, E.; Dincer, I. Energy and exergy analyses of a combined ammonia-fed solid oxide fuel cell system for vehicular applications. *Int. J. Hydrogen Energy* **2011**, *36*, 11128–11136.
23. Sørensen, R.Z.; Hummerlshøj, J.S.; Klerke, A.; Reves, J.B.; Vegge, T.; Nørskov, J.K.; Christensen, C.H. In direct, reversible high-density hydrogen storage in compact metal ammine salts. *J. Am. Chem. Soc.* **2008**, *130*, 8660–8668.
24. Olovosson, I. Packing Principles in the Structures of Metal Ammine Salts. *Acta. Crystallogr.* **1965**, *18*, 889–893.
25. Eβmann, R.; Kreiner, G.; Niemann, A.; Rechenbach, D.; Schmieding, A.; Sichla, T.; Zachwieja, U.; Jacobs, H. The Structures of some Hexaammine Metal(II) Halides of 3d Metals: $[V(NH_3)_6]I_2$, $[Cr(NH_3)_6]I_2$, $[Mn(NH_3)_6]Cl_2$, $[Fe(NH_3)_6]Cl_2$, $[Fe(NH_3)_6]Br_2$, $[Co(NH_3)_6]Br_2$, $[Ni(NH_3)_6]Cl_2$. *Z. Anorg. Allg. Chem.* **1996**, *622*, 1161–1166.
26. Wentworth, W.E.; Raldrow, W.M.; Corbett, G.E. Correlation of Thermodynamic Properties for Dissociation of Ammines of Divalent Metal Halides. *Inorg. Chem. Acta* **1978**, *30*, L299–L301.

27. Lepinasse, E.; Spinner, B. Cold production through coupling of solid-gas reactors I: Performance analysis. *Rev. Int. Froid* **1994**, *17*, 309–322.
28. Biltz, W.; Hüttig, G.F. Über die Ammoniakate der Magnesiumhalogenide. *Z. Anorg. Allg. Chem.* **1921**, *119*, 115–131.
29. Schmidt, H.; Müller, A. Skeletal Vibrational Spectra, Force Constants, and Bond Properties of Transition Metal Ammine Complexes. *Inorg. Chem.* **1975**, *14*, 2183–2187.
30. Schmidt, H.; Müller, A. Vibrational Spectra and Force Constants of Pure Ammine Complexes. *Coord. Chem. Rev.* **1976**, *19*, 41–97.
31. Sacconi, L.; Sabatini, A.; Gans, P. Infrared Spectra from 80 to 2000 Cm^{-1} of Some Metal-Ammine Complexes. *Inorg. Chem.* **1964**, *3*, 1772–1774.
32. Larkin, P. IR and Raman spectra—Structure Correlations: Characteristic Group Frequencies. In *Infrared and Raman Spectroscopy*, 1st ed.; Elsevier: Amsterdam, The Netherlands, 2011; Chapter 6, pp. 73–115.
33. Plus, R. Spectroscopie Raman de $Mg(NH_3)_6Cl_2$ et $Mg(ND_3)_6Cl_2$. *J. Raman Spectrosc.* **1973**, *1*, 551–563.
34. Jacobs, H.; Brock, J.; Stüve, C. Rontgenographische Strukturbestimmung und IR-Spektroskopische Untersuchungen an Hexaammindiiodiden, $[M(NH_3)_6I_2]$, von Eisen und Mangan. *J. Less-Common. Met.* **1987**, *134*, 207–214.
35. Schiebel, P.; Hoser, A.; Prandl, W.; Heger, G.; Schweiss, P.Orientational disorder in $Ni(NH_3)_2I_2$. Evidence for rotation-translation coupling. *J. Phys. I. France* **1993**, *3*, 987–1006.
36. Schiebel, P.; Hoser, A.; Prandl, W.; Heger, G.; Paulus, W.; Schweiss, P. Proton density and orientational potential in nickelhexammine salts: a thermodynamic analysis of rotation-translation coupling. *J. Phys. Condens. Matter* **1994**, *6*, 10989–11005.
37. Watt, M.; Manhas, B.S. Replacement of polydentate ligands in Mn(II) complexes by ammonia. *J. Inorg. Nucl. Chem.* **1966**, *28*, 1945–1947.
38. Kraus, W.; Nolze, G. POWDER CELL—a program for the representation and manipulation of crystal structures and calculation of the resulting X-ray powder patterns. *J. Appl. Cryst.* **1996**, *29*, 301–303.
39. Schefer, J.; Schwarzenbach, D.; Fischer, P.; Koetzle, T.; Larsen, F.K.; Haussühl, S.; Rüdlinger, M.; McIntyre, G.G.; Birkedal, H.; Bürgi, H.-B. Neutron and X-ray Diffraction Study of the Thermal Motion in K_2PtCl_6 as a function of Temperature. *Acta Crystallogr.* **1998**, *B54*, 121–128.
40. Shannon, R.D. Revised Effective Ionic Radii and Systematic Studies of Interatomic Distances in Halides and Chalcogenides. *Acta Crystallogr.* **1976**, *A32*, 751–767.
41. Leineweber, A.; Friedriszik, M.W.; Jacobs, H. Preparation and Crystal Structures of $Mg(NH_3)_2Cl_2$, $Mg(NH_3)_2Br_2$, $Mg(NH_3)_2I_2$. *J. Solid State Chem.* **1999**, *147*, 229–234.
42. Leineweber, A.; Jacobs, H.; Fischer, P.; Böttger, G. Uniaxial Orientational Order-Disorder Transitions in Diammine Magnesium Halides, $Mg(ND_3)_2Cl_2$ and $Mg(NH_3)_2Br_2$, Investigated by Neutron Diffraction. *J. Solid State Chem.* **2001**, *156*, 487–499.
43. Leineweber, A.; Jacobs, H.; Ehrenberg, H. Crystal Structure of $Ni(NH_3)Cl_2$ and $Mg(NH_3)Br_2$. *Z. Anorg. Allg. Chem.* **2000**, *626*, 2146–2152.

44. Barker, M.G.; Begley, M.J.; Edwards, P.P.; Gregory, D.H.; Smith, S.E. Synthesis and crystal structures of the new ternary nitrides Sr_3CrN_3 and Ba_3CrN_3. *J. Chem. Soc., Dalton Trans.* **1996**, *11*, 1–5.
45. Laugier, J.; Bochu, B. ENSP/Laboratoire des Matériaux et du Génie Physique, LMGP-Suite Suite of Programs for the Interpretation of X-ray Experiments. Available online: http://www.inpg.fr/LMGP and http://www.ccp14.ac.uk/tutorial/lmgp/ (accessed on 20 February 2012).
46. Larson, A.C.; von Dreele, R.B. *General Structure Analysis System (GSAS)*; Los Alamos National Laboratory Report LAUR: 86-748, Los Alamos, NM, USA, 1995.
47. Toby, B.H. EXPGUI, a graphical user interface for GSAS. *J. Appl. Cryst*. **2001**, *34*, 210–213.